ACS APPLIED MATERIALS & INTERFACES

www.acsami.org

Research Article

Label-Free Electrochemical Immunosensor for Ultrasensitive Detection of Carbohydrate Antigen 125 Based on Antibody-Immobilized Biocompatible MOF-808/CNT

Sudip Biswas,* Qingchun Lan, Yao Xie, Xin Sun, and Yang Wang

Cite This: *ACS Appl. Mater. Interfaces* 2021, 13, 3295−3302

Read Online

ACCESS | Metrics & More | Article Recommendations | Supporting Information

ABSTRACT: In this work, a nanocomposite of Zr-trimesic acid MOF (MOF-808) with carbon nanotube (CNT) was synthesized through an in situ formation of MOF-808 on the activated CNT. The synthesized materials were characterized by powder X-ray diffraction, transmission electron microscopy, X-ray photoluminescence spectroscopy, Brunauer−Emmett−Teller, Fourier transform infrared spectroscopy, and Raman spectroscopy. The protein compatible nature with high surface area and electrocatalytic ability of MOF-808 was utilized to construct an immunosensor for ultra low-level detection of the ovarian cancer biomarker, carbohydrate antigen 125 (CA 125). The mutual benefit of each constituent of the MOF-808/CNT composite was capable of producing highly enhanced electrochemical properties. A glassy carbon electrode modified with MOF-808/CNT was used as a platform to fabricate a label-free electrochemical immunosensor. The antibody binding sites of MOF-808/CNT were enriched by functionalization with streptavidin. The immunosensor exhibited two linear determination ranges of 0.001−0.1 and 0.1−30 ng·mL^{-1}, and the calculated limit of detection was 0.5 pg·mL^{-1} (S/N 3). The immunosensor showed excellent reproducibility and selectivity. The patient serum sample analysis was cross-verified with the electrochemiluminescence method with a relative error of 105−110%.

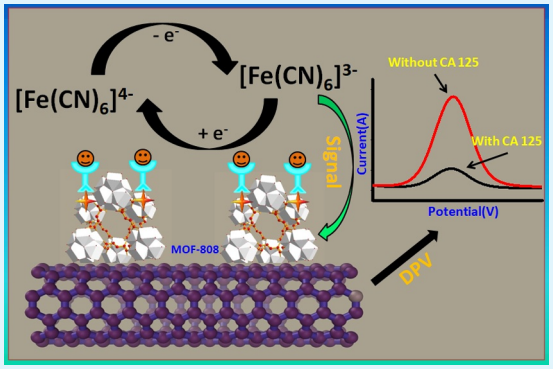

KEYWORDS: *metal−organic framework, MOF-808, biosensor, cancer diagnosis, immobilization, streptavidin*

Downloaded via RUTGERS UNIV on May 15, 2021 at 10:03:38 (UTC).
See https://pubs.acs.org/sharingguidelines for options on how to legitimately share published articles.

1. INTRODUCTION

Ovarian cancerous tumor shows external symptoms in advanced stages.[1] The epithelial antigen, carbohydrate antigen 125 (CA 125), is a biomarker protein for cancer, especially ovarian cancer.[2] Therefore, simple, low-cost trace level detection of CA 125 has potential importance in the routine clinical screening for early detection and prognosis of ovarian cancer. Many attempts have been made for the detection of CA 125 using different approaches such as enzyme-linked immunosorbent assays,[3,4] surface plasmon resonance,[5] colorimetry,[6] mass spectroscopy,[7] and so forth. Each of these methods has pros and cons. Here, we have used an electrochemical immunosensor because of its simplicity, high inherent sensitivity, and portability. Immunosensors are robust sensing and monitoring tools with high specificity.[8] The quest is on for sensor signal amplification using advanced material platforms for the electrochemical immunosensor to detect protein biomarkers in clinical samples.[9,10] The electrochemical immunosensor platform based on advanced materials with biocompatibility, electrical conductivity, and high surface area with enhanced electrocatalytic activity can produce better analytical performances in all terms for clinical sample analysis. Till now various materials were used as a base for the fabrication of immunosensor or immunoassay transducers viz. Au,[11] Ag nanoparticles,[12] conducting carbon polymer,[13] porous silica,[14] graphene composites,[15] and carbon nanotube (CNT) composites.[16]

Metal−organic framework (MOF) is a coordination polymer, made of the consecutively linked organic linker with the inorganic metal ion in a highly oriented structure. It has some fascinating properties such as an ultra-high surface area with abundant tunable pores, dense catalytic sites, and appropriate functional groups at the surface.[17−19] However, MOFs are inherently poor conductors and have low stability in water medium. Currently, huge progress has been made to synthesize new stable MOFs, investigating their applications in the field of different catalytic processes, gas adsorption/separation, supercapacitors, chemical sensors, fuel cells, and

Received: August 19, 2020
Accepted: December 23, 2020
Published: January 5, 2021

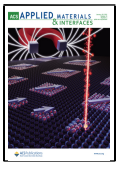

ACS Publications

© 2021 American Chemical Society

batteries.[20−22] However, there has been little research on the protein molecule immobilization on the MOF matrix for the electrochemical immunosensor. MOFs can incorporate biomolecules and even enhance their stability and activity.[23−25]

MOF-808 is highly stable, and it has shown an effective affinity toward protein molecules[25,26] because of the large coordination numbers, flexible geometries, oxophilicity, and increased Lewis acidity of Zr(IV).[27] It is composed of $[Zr_6O_4(\mu_3\text{-}OH)_4(formate)_6]$ clusters and trimesic acid (BTC^{3-}) linkers. According to the previously reported[27−29] work, the "formate" within the zirconium clusters can be replaced by the treatment with 1 M HCl to coordinate −OH and H_2O ligands. Consequently, all of the $Zr-OH(OH_2)$ sites in MOF-808 should also be available through the large hexagonal windows to form an adduct with carboxylate or nonbonded electron pair present in the protein structure.[28]

Based on the above discussions, here we have enhanced the electrical conductivity of MOF-808 by making a composite with a multiwall CNT. The synthesized MOF-808/CNT was used to fabricate a label-free electrochemical immunosensor for CA 125. The biosensor working principle is based on the distinguishing hindrance created by specific antibody−antigen binding on mass diffusion of redox probe $[Fe(CN)_6]^{4-}$/$[Fe(CN)_6]^{3-}$ to the electrode surface. The MOF-808/CNT modified GCE electrode can produce appropriate high density immobilizing sites from $Zr-OH(OH_2)$ and enhanced interfacial charge transfer through the CNT backbone. The anti-CA 125 binding sites were heightened by functionalization with streptavidin (SA) on the MOF-808/CNT surface. The combined merits of each constituent of MOF-808/CNT lead to the generation of a biocompatible surface with enhanced electrochemical properties. The analytical methods were optimized to get better performances for the detection of CA 125 in terms of linear determination range, sensitivity, selectivity, reproducibility, and finally successful application in the practical sample.

2. EXPERIMENTAL SECTION

2.1. Preparation of Activated CNT. 500 mg of CNT was added to an 80 mL mixture of 3:1 (v/v) concentrate H_2SO_4 and HNO_3. The mixture was stirred for 1 h at room temperature. Then, 500 mL of cold Millipore water was added carefully without forming excess heat and was stirred for another 2 h. Once the residue settled down, the clear upper part was decanted out. This process was done three times. Then, the activated CNT (AC-CNT) was collected by centrifugation at 10,000 rpm and washed with 10 mL of distilled water three times. Finally, the obtained AC-CNT was dried at 70 °C in a hot air oven.

2.2. Synthesis of MOF-808. MOF-808 was synthesized by the method reported elsewhere with some modifications.[29] Briefly, 0.1747 mg of anhydrous $ZrCl_4$ (0.75 mM) and 0.0525 mg of trimesic acid (0.25 mM) were added to a 45 mL of 1:1 (v/v) binary mixture of formic acid and *N*,*N*′-dimethylformamide (DMF) in a 250-mL round-bottom flask. Then, the whole mixture was sonicated for 10 min, and a clear solution was formed. After that, it was refluxed at 140 °C for 2 h, followed by cooling down at room temperature. The obtained white precipitate was washed with DMF (10 mL × 3) and methanol (10 mL × 3) by centrifugation at 8000 rpm. The collected white residue was dried at 70 °C for 12 h in vacuum.

2.3. Synthesis of MOF-808/CNT. 100 mg of AC-CNT was added to 60 mL of 1:1(v/v) binary mixture of formic acid and DMF. A uniform dispersion was obtained by sonication for 30 min. Then, 0.1747 mg of anhydrous $ZrCl_4$ (0.75 mM) and 0.0525 mg of trimesic acid (0.25 mM) were added to the above dispersion and sonicated for another 30 min followed by reflux for 2 h at 140 °C. The obtained grey mass was collected (8000 rpm) and washed with DMF (10 mL × 4) and methanol (10 mL × 3), followed by vacuum drying at 70 °C for 12 h. The amount of CNT was optimized to get the best performance (Figure S1).

2.4. Activation of MOF-808/CNT and MOF-808. 250 mg of the synthesized materials (MOF-808/CNT or MOF-808) were taken in a 100-mL round-bottom flask. After that, 55 mL of DMF and 5 mL of concentrated HCl were added. The obtained suspension was sonicated for 5 min followed by incubation at 80 °C for 24 h. After that, the suspension was cooled down to room temperature and washed with DMF (10 mL × 3) and methanol (10 mL × 2). The obtained grey powder was dried at 80 °C in vacuum.

2.5. Preparation of the Electrode. The bare GCEs were polished with 0.3 μm followed by 0.05 μm α-Al_2O_3 slurries on chamois leather to make a mirrorlike surface. After that, the polished GCEs were sonicated in ethanol, followed by distilled water for 2 min to clean the surface of any possible particle adhering to the surface. Finally, 10 μL of 1 mg·mL^{-1} MOF-808/CNT or CNT or MOF-808 dispersed in 5% (w/w) chitosan solution was added dropwise on the surface of GCEs and dried in desiccators at room temperature.

2.6. Electrochemical Measurements. All the electrochemical experiments were done by a three-electrode setup. The used three-electrode system includes a Pt counter electrode, a KCl saturated Ag/AgCl reference electrode, and a GCE working electrode. The GCE modification and all the functionalization steps were monitored by cyclic voltammetry (CV) and electrochemical impedance spectroscopy (EIS). The linear determination ranges were investigated by differential pulse voltammetry (DPV), after nonspecific sites of the fabricated sensor bovine serum albumin (BSA)-blocked electrodes were incubated with 10 μL of CA 125 solution with different concentrations by dipping the electrodes in a 5 mM $[Fe(CN)_6]^{3-}$/$[Fe(CN)_6]^{4-}$ solution with 0.1 M KCl. The quantitative analysis was examined by a decrease in the peak current of DPV with the increase of the CA 125 concentration. The parameters for DPV measurements were as follows: the potential range −0.2 to 0.6 V, potential increment 0.004 V, pulse amplitude 0.05 V, the pulse width 0.2 s, sample width 0.0167 s, and the pulse period 0.5 s.

2.7. Fabrication of the Immunosensor. The complete fabrication produced is presented graphically in Scheme 1. 10 μL of 200 μg·mL^{-1} SA aqueous solution was added dropwise on the MOF-808/CNT/GCE. 30 min later, it was washed with phosphate-buffered saline (PBS) of pH 7.0 and air-dried. Then, 10 μL of 10 μg·mL^{-1} of anti-CA 125 was added dropwise on SA/MOF-808-CNT/GCE and incubated for 30 min at 26 °C and finally washed carefully with PBS (pH 7.0). After that, the anti-CA 125/SA/MOF-808/CNT/GCE electrode was incubated with 10 μL of BSA (1% w/w) for 40 min at 26 °C to cover the nonbounded open active sites and washed with PBS (pH 7.0). Finally, the electrode was incubated with 10 μL of different concentrations of CA 125 for 25 min at 26 °C, followed by washing with PBS and then measuring the electrochemical signals. All the experimental conditions were optimized to get the best result.

Scheme 1. Illustration of Stepwise Fabrication of the Immunosensor

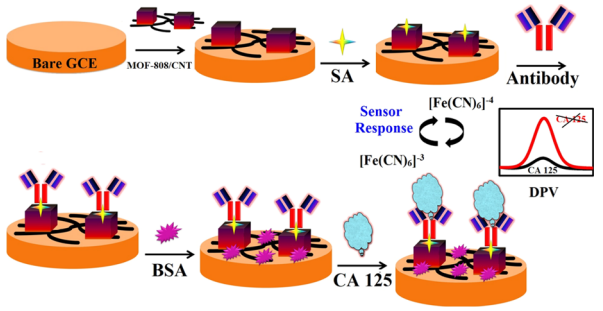

https://dx.doi.org/10.1021/acsami.0c14946
ACS Appl. Mater. Interfaces 2021, 13, 3295−3302

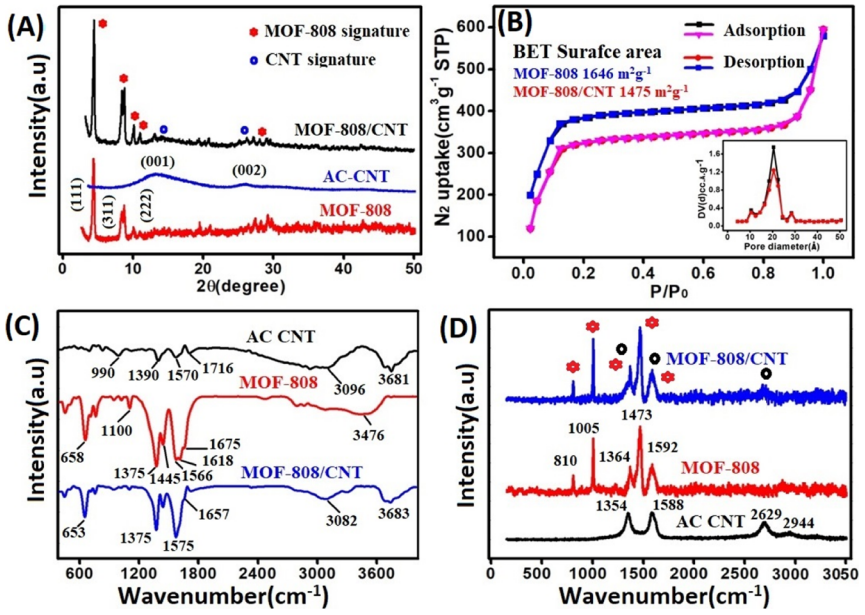

Figure 1. (A) PXRD pattern and (B) nitrogen adsorption and desorption isotherms measured at 77 K. Inset: pore size distribution; (C) FTIR; and (D) Raman spectrum.

3. RESULTS AND DISCUSSION

3.1. Characterization. The crystalline nature and the successful synthesis of MOF-808, MOF-808/CNT, and AC-CNT were investigated by powder X-ray diffraction (PXRD) technique (Figure 1A). Both MOF-808 and MOF-808/CNT showed sharp peaks indicating the formation of a highly crystalline structure. The PXRD pattern of MOF-808 showed the peaks at 4.4, 8.3, and 8.7° corresponding to (111), (311), and (222) crystalline plane. This is in good agreement with the previously reported work.[28−30] The diffraction pattern of the activated CNT showed a shift and broad peak compared to the pristine CNT of the (001) and (002) plane peaks. This is due to the formation of a carboxylate group upon oxidation.[31] A combined pattern of individual peaks was observed in the case of the composite material, MOF-808/CNT.

The specific surface area of MOF-808 and MOF-808/CNT was analyzed after activation by the Brunauer−Emmett−Teller (BET) method. The nitrogen adsorption−desorption isotherms of MOF-808 and MOF-808/CNT are presented in Figure 1B. Both the synthesized materials showed a type-IV curve.[32] This is a common phenomenon for mesoporous materials. The BET surface areas of MOF-808 and MOF-808/CNT were found as 1646 and 1475 $m^2 \cdot g^{-1}$, respectively. The pore diameter was calculated using the Barrett−Joyner−Halenda method. The value of the pore diameter for both the materials was 2.1 nm.

The successful synthesis of each material was investigated by Fourier transform infrared spectroscopy (FTIR) (Figure 1C). The AC-CNT showed typically two sets of the band from 900−1730 to 2700−3800 cm^{-1}. In the first region, the peak at 1570 cm^{-1} is attributed to the CNT backbone and all other bands represent the carboxylate group produced by the oxidation of nitric acid.[31] The second part contains two peaks attributed to O−H groups. The FTIR spectrum of MOF-808 contains the signature peak at 658 cm^{-1} for the Zr−O bond in Zr nodes. The peaks from 1375 to 1675 cm^{-1} were generated because of the carboxylate groups and the aromatic rings within the trimesic acid ligands. The broadband at 3476 cm^{-1} is attributed to the replaceable −OH groups attached to Zr nodes. Finally, the MOF-808/CNT FTIR spectrum contains the combined nature of both the constituents with an overlap of the slightly shifted peaks. This indicates the successful formation of the MOF-808/CNT composite. The Raman spectra (Figure 1D) of AC-CNT consisted of typical D (1354 cm^{-1}) and G (1588 cm^{-1}) peaks with an overtone of G-mode, namely, 2D (2629 cm^{-1}). The small peak at 2944 cm^{-1} originated from the defects formed by oxidation. The spectrum of MOF-808 showed peaks mainly corresponding to the trimesic acid ligands. The peak at 810 cm^{-1} is attributed to the out-of-plane deformative mode of C−H groups. The peaks at 1005, 1364, and 1592 cm^{-1} come from the aromatic C═C mode of vibration. The intense sharp big peak at 1473 cm^{-1} corresponds to the CO_2^- groups. The spectral signature of composites, MOF-808/CNT contains overlapped and combined peaks of both the constituents. All these discussions collectively indicate the successful formation of the nanocomposite between MOF-808 and CNT.

The morphology of the synthesized materials was examined by scanning electron microscopy (SEM) and transmission electron microscopy (TEM). SEM of MOF-808 depicted nanometer-sized cubic-shaped particles (Figure 2A). This is also supported by TEM (Figure 2B). The MOF-808/CNT showed a cubic MOF-800 anchored on the CNT matrix (Figure 2C). The size of the MOF particle in the MOF-808/CNT is relatively smaller than the individual MOF-808. The TEM image showed the formation of MOF cubes along the CNTs (Figure 2D). The EDX mapping images show that Zr, C, and O are distributed uniformly over the entire architecture (Figure 2F−H). The CNT in the HAADF-STEM image (Figure 2F) and C-mapped image is in good correlation. All these above discussions imply the successful synthesis of MOF-808 and CNT composites.

3.2. Electrochemical Studies. The electrochemical properties of the MOF-808-modified GCE (MOF-808/GCE) were investigated by CV and EIS (Figure S2a,b), and the obtained results were compared with the same of the CNT-

https://dx.doi.org/10.1021/acsami.0c14946
ACS Appl. Mater. Interfaces 2021, 13, 3295−3302

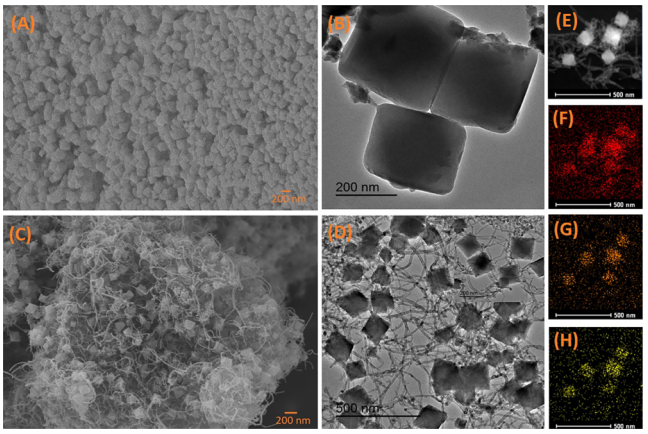

Figure 2. SEM images of (A) MOF-808 and (C) MOF-808/CNT; TEM images of (B) MOF-808 and (D) MOF-808/CNT; and (E–H) HAADF-STEM image (scale bar: 500 nm) and EDX elemental mapping.

modified GCE (CNT/GCE) and bare GCE. The CV redox peak currents were increased at MOF-808/CNT/GCE compared to bare GCE and CNT/GCE by 2.8 and 1.5 times, respectively. The charge transfer capabilities of the electrodes were investigated by EIS. The impedance spectrum is commonly presented in the form of the Nyquist plot, which is composed of the semicircle portion at higher frequencies and the linear portion at lower frequencies.[33] The semicircle diameter of the Nyquist plot can be quantified as the charge transfer resistance (R_{ct}). The R_{ct} value for the bare GCE, CNT/GCE, and MOF-808/CNT/GCE was found as 131, 47, and 81 Ω, respectively. The electrochemical surface area of the electrodes was calculated by the Randles–Sevcik equation[34] (Supporting Information, Table S1). It was found that the MOF-808/CNT/GCE possesses a larger electrochemical surface area (0.243 cm^2) and charge transfer capability among these three electrodes. All these results can be attributed to the combination of high electrical conductive CNT with a high specific surface area and densely populated Zr nodes catalytic sites of the MOF-808. All these characteristics with an inherently protein compatible environment at the MOF-808 should facilitate the noncovalent attachment of the biomolecules on the electrode surface and enhance the sensor signal.

Each step of the immunosensor fabrication was characterized by CV, EIS, X-ray photoluminescence spectroscopy (XPS), and static contact angle measurements (Figure 3). CVs and EIS were done in the presence of 5 mM $[Fe(CN)_6]^{3-}/[Fe(CN)_6]^{4-}$ with 0.1 M KCl. One SA can form selective, noncovalent bonding with four biotin moieties. Owing to this fact, the biotinylated antibody was used. Each biomolecular immobilization on the MOF-808/CNT/GCE increments hindrance on the mass diffusion of $[Fe(CN)_6]^{3-}/[Fe(CN)_6]^{4-}$ at the electrode surface and degrades charge transfer. Eventually, it leads to a decrease in the peak current and an increase in charge transfer resistance by each fabrication step. CV for each immobilization is presented in Figure 3A. Upon each consecutive immobilization of biomolecules on the MOF-808/CNT/GCE, the redox peak currents were decreased in the order as follows: (b) MOF-808/CNT/GCE > (c) SA/MOF-808/CNT/GCE > (d) anti-CA 125/SA/MOF-808/CNT/GCE > (e) BSA/antibody/SA/MOF-808/CNT/GCE > (f) CA 125/BSA/antibody/SA/MOF-808/CNT/GCE. This is according to the anticipated order with the respective immobilization steps. The result of the EIS measurements is presented in Figure 3B. The Nyquist plots showed that the R_{ct} value increased upon consecutive immobilization on the MOF-808/CNT/GCE platform with (c) SA (166 Ω) < (d) anti-CA 125 (238 Ω) < (e) BSA (272 Ω) < (f) CA 125 (307 Ω). The EIS outcome is in good correlation with CV investigation. The immunosensor fabrication process was further verified with the static contact water angle measurement at ambient temperature by the sessile drop method. The protein compatibility of the platform depends on the hydrophobicity. Figure S3 shows the contact angle of (a) bare GCE (66.9°), (b) MOF-808/CNT/CGE (47.5°), (c) SA/MOF-808/CNT/CGE (39.7°), and (d) anti-CA 125/SA/MOF-808/CNT/CGE (31.4°). The hydrophobic MOF-808/CNT leads to a decrease in the contact angle value as compared to the bare GCE. The biomolecules, SA, and anti-CA 125 are reasonably hydrophobic. Further decrease in the contact angle was observed for obvious reasons. The hydrophobic environment of the biosensor can provide a favorable bioactive environment for the loaded antibody molecules. The XPS investigation of the immunosensor fabrication process showed an incremental increase in the N 1s peaks (Figure S4) upon each biomolecule functionalization step. This indicates successful immobilization of the biomolecules. The XPS observations are consistent with the CV, EIS, and static contact angle measurement. Therefore, all the above discussion indicates the successful fabrication of the targeted immunosensor.

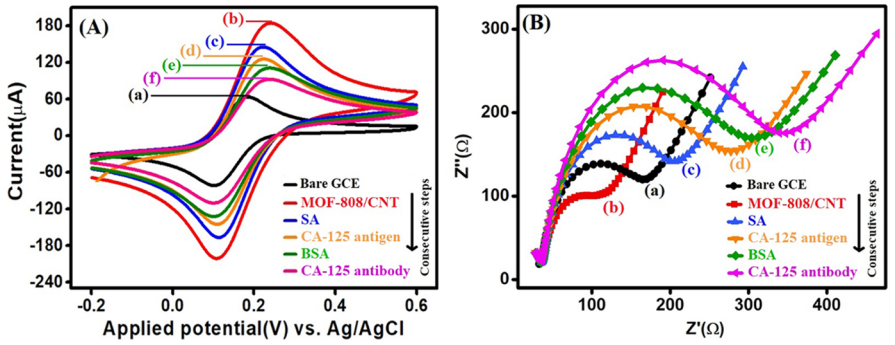

Figure 3. (A) CVs and (B) EIS plots of different biomolecules functionalized steps at MOF-808/CNT/GCE in 5 mM $[Fe(CN)_6]^{3-/4-}$ containing 0.1 M KCl at a pH of 7.0 PBS; (a) bare GCE, (b) MOF-808/CNT/GCE, (c) SA/MOF-808/CNT/GCE, (d) anti-CA 125/SA/MOF-808/CNT/GCE, (e) BSA/anti-CA 125/SA/MOF-808/CNT/GCE, and (f) CA 125/BSA/anti-CA 125/SA/MOF-808/CNT/GCE.

https://dx.doi.org/10.1021/acsami.0c14946
ACS Appl. Mater. Interfaces 2021, 13, 3295–3302

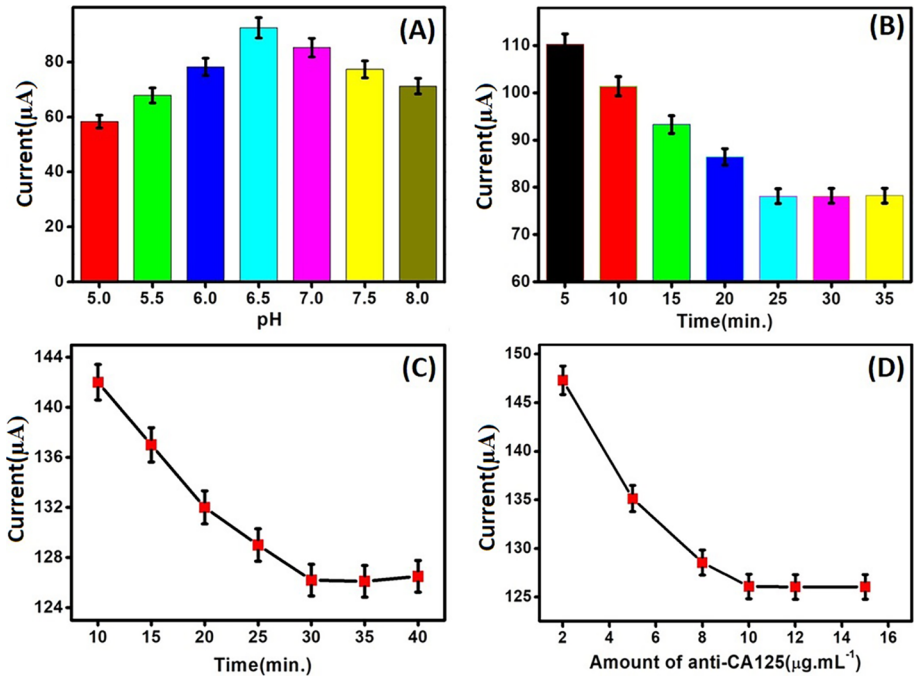

Figure 4. (A) Variation of CV anodic peak current with pH; (B) optimization of incubation time for antigen; (C) antibody binding time optimization; and (D) amount of antibody optimization (n = 4 for each point).

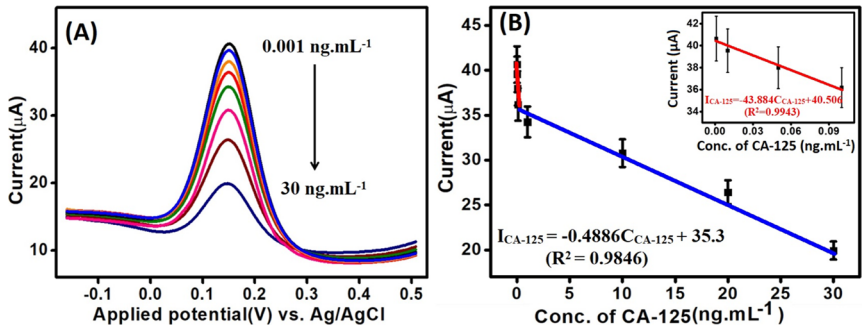

Figure 5. (A) Differential pulse voltammograms of different concentration of CA 125 incubated immunosensor in 5.0 mM $[Fe(CN)6]^{3-}$/$[Fe(CN)6]^{4-}$ solution with 0.1 M KCl; top to bottom 0.001, 0.001, 0.05, 0.1, 1.0, 10, 20, and 30 ng·mL^{-1} and (B) corresponding calibration plot concentration of CA 125 (ng·mL^{-1}) vs peak current (μA).

3.3. Optimization of Immunosensor. Various parameters of the immunosensor fabrication process were optimized (Figure 4). The optimal assay for the immunosensor fabrication was done by the CV current signal of the immunosensor in PBS solution containing 5.0 mM $[Fe(CN)_6]^{3-}$/$[Fe(CN)_6]^{4-}$ containing 0.1 M KCl. The electrochemical process and protein structure highly depend on the medium pH. The immunosensor showed the highest current value at a pH of 6.5 in 0.1 M PBS (Figure 4A). However, all the experiments were carried out at a pH of 7.0 since the protein structures and immune complex stability are highly sensitive to medium pH. The incubation time is an important parameter, as it can enhance the sensitivity and fasten the fabrication process. The incubation time was investigated using 30 ng·mL^{-1} CA 125. Figure 4B shows a gradual decrease in the anodic peak current with increasing incubation time up to 25 min and becomes steady afterward. Also, the amount of anti-CA 125 and its binding time with SA/MOF-808/CNT were optimized (Figure 4C,D). These are vital factors for the immunological reorganization of CA 125. 2 μg·mL^{-1} of anti-CA 125 showed the highest effective blocking toward the penetration of the redox probe upon adduct formation with SA (Figure 4D). The optimum binding time of anti-CA 125 with SA was found as 30 min (Figure 4C). Figure 4B–D shows a similar kind of pattern. In each case, the minima of current values were reached by the highest blocking in mass transfer owing to the surface binding. Also, there was a slight increase in current after maxima in the above three cases. This is due to the formation of a scabrous and uneven electrode surface by superabundant agglomerations of antibody/antigen. All further experiments were performed according to these optimized conditions.

3.4. Voltammetric Determination of CA 125. The quantitative measurement of CA 125 was done by incubating different concentrations of CA 125 on the immunosensor. DPV was employed to examine the analytical capabilities of the fabricated immunosensor under optimized conditions (Figure 5). Figure 5A displays typical DPV detection of CA 125 in the presence of $[Fe(CN)_6]^{3-/4-}$ probe. It can be noted that the DPV peak currents were decreased with an increase in the CA 125 concentrations. This is due to the increased formation of immunoconjugates on the immunosensor; as a consequence,

https://dx.doi.org/10.1021/acsami.0c14946
ACS Appl. Mater. Interfaces 2021, 13, 3295−3302

Table 1. Comparison of Analytical Performances

material	method	determination range ($ng \cdot mL^{-1}$)	detection limit ($ng \cdot mL^{-1}$)
carbon dots[35]	fluorescence	0.000001−1	0.000005
AgNPs/GQD[12]	electrochemical	0.01−400	0.01
Au nanorod[36]	plasmon resonance	1−80	0.4
Ru-AuNPs/GR[37]	electrochemiluminescence	0.01−100	0.005
hollow PDA-Au NPs[38]	colorimetry	1−100	0.1
GO/thionine/Au NPs[39]	electrochemical	0.1−200	0.01
MOF-808/CNT (this work)	**electrochemical**	**0.001−30**	**0.0005**

there is an incremental growth of hindrance toward the mass transfer of the redox probe. The DPV oxidation current was found to follow a linear relationship with the concentration of CA 125 within the range of 0.001−0.1 and 0.1−30 $ng \cdot mL^{-1}$ with the linear regression eqs 1 and 2 (Figure 5B). The limit of detection was calculated as 0.0005 $ng \cdot mL^{-1}$ (S/N 3). These results indicate the excellent analytical performance of the fabricated biosensor. Furthermore, the obtained analytical performance was compared with the previously reported immunosensor and is presented in Table 1. Various reported immunosensors and methodology were included. The analytical performances were better compared to the other immunosensors. Especially the detection limit was better by decimal places.

$$I_{\text{CA 125}} = -43.884C_{\text{CA 125}} + 40.506 \qquad (R^2 = 0.9943) \tag{1}$$

$$I_{\text{CA 125}} = -0.4886C_{\text{CA 125}} + 35.3 \qquad (R^2 = 0.9846) \tag{2}$$

3.5. Evaluation of Reproducibility, Selectivity, Stability, and Application. To examine the reproducibility of the fabricated sensor, ten immunosensors were incubated with 10 $ng \cdot mL^{-1}$ of CA 125, and DPVs were recorded in a 5.0 mM $[Fe(CN)_6]^{3-}/[Fe(CN)_6]^{4-}$. The relative standard deviation (RSD) for the measurements was calculated to be 2.2%. The carcinoembryonic antigen, human IgG, α-fetoprotein, glucose, and CA 19-9 were used as interferers to examine the selectivity. Figure S5 shows a negligible decrease in the DPV peak current, less than 5%, for the taken interferers compared to only CA 125. This is attributed to the high selectivity of the fabricated sensor toward CA 125. To evaluate the specificity, the proposed immunosensor was incubated with 10 $ng \cdot mL^{-1}$ of each interfering agent, followed by measuring using DPV. Figure S6 shows that the peak current of DPV toward the interfering substances was close to the response of the blank solution. However, the peak current for CA 125 (30 $ng \cdot mL^{-1}$) was much lower than that of the interfering substances. To estimate the stability, the immunosensors were stored at 4 °C for 9 weeks while examining and measuring the CA 125 every week (Figure S7). The immunosensor showed a negligible decrease in the peak current (RSD 3.1). The results demonstrated that the designed immunosensor has satisfactory reproducibility, selectivity, and stability.

The practical applicability of the fabricated immunosensor was investigated by measuring CA 125 within the patient serum samples collected from Yangzhou University Hospital and stored at 4 °C. 1 mL of serum sample was diluted 20 times with PBS (pH 7.0) for stock (Figure S8 and Table S2). The RSD for the serum analysis was between 97 and 103%. Furthermore, the validity of the measured amount of CA 125 in the serum samples was cross-examined with the ECL immunoassay reference method, which was conducted by Yangzhou University Hospital. The obtained results showed an acceptable relative error within 10% between these two methods. Therefore, the fabricated immunosensor was highly effective for the diagnosis of a clinical sample.

4. CONCLUSIONS

Here, we have demonstrated a SA-functionalized MOF-808/CNT-based label-free electrochemical immunosensor platform for CA 125 ovarian cancer biomarker detection. The target for the improvement of MOF-808's electroconductivity and catalytic activity was achieved successfully by making a composite with the CNT. The MOF-808/CNT-modified GCE exhibited high electrochemical surface area (0.243 cm^2), excellent charge transfer, and electrocatalytic properties. Furthermore, the combination of biocompatibility and fascinating electrochemical properties of MOF-808/CNT produced an advanced immunoassay fabrication platform for label-free CA 125 detection. This immunoassay strategy can be easily achieved by immobilization of the captured antibodies on MOF-808/CNT through a biotin-avidin system. Also, the immunosensor showed a lower incubation time without losing sensitivity. The developed immunosensor showed a wide linear determination range (0.001−30 $ng \cdot mL^{-1}$) under the optimized condition with the highest sensitivity (43.88 $\mu A \cdot ng^{-1} \cdot mL^{-1}$) and an ultra-low detection limit of 0.5 $pg \cdot mL^{-1}$. In terms of sensor properties, the fabricated sensor is reasonably reproducible (RSD 99.3%), selective, and robust. The patient serum sample analysis with the recovery of 105−110% indicates that the fabricated sensor has a great potential for clinical application. The MOF-808/CNT provides a universal and promising avenue for the development of immunoassay applications.

■ ASSOCIATED CONTENT

Supporting Information

The Supporting Information is available free of charge at https://pubs.acs.org/doi/10.1021/acsami.0c14946.

Instrumentation and apparatus, chemicals, calculation of electrochemical properties of the materials, tables, and figures related to material optimization, XPS, static contact angle measurement, specificity, reproducibility, robustness, selectivity, real sample analyses, and comparison with the standard clinical method (PDF)

■ AUTHOR INFORMATION

Corresponding Author

Sudip Biswas − *College of Chemistry & Chemical Engineering, Yangzhou University, Yangzhou 225002, P. R. China;* orcid.org/0000-0003-0268-1703; Email: sudipbiswas65@gmail.com

https://dx.doi.org/10.1021/acsami.0c14946
ACS Appl. Mater. Interfaces 2021, 13, 3295−3302

Authors

Qingchun Lan − *College of Chemistry & Chemical Engineering, Yangzhou University, Yangzhou 225002, P. R. China*

Yao Xie − *College of Chemistry & Chemical Engineering, Yangzhou University, Yangzhou 225002, P. R. China*

Xin Sun − *College of Chemistry & Chemical Engineering, Yangzhou University, Yangzhou 225002, P. R. China*

Yang Wang − *College of Chemistry & Chemical Engineering, Yangzhou University, Yangzhou 225002, P. R. China*

Complete contact information is available at: https://pubs.acs.org/10.1021/acsami.0c14946

Author Contributions

Conceptualization of the work and the complete manuscript writing were done by S.B. All authors have approved the final version of the manuscript.

Notes

The authors declare no competing financial interest.

■ ACKNOWLEDGMENTS

This work was supported by the Jiangsu Postdoc Foundation of China (217744) and Yangzhou University Postdoc Fund (007124).

■ REFERENCES

(1) Hamilton, W.; Peters, T. J.; Bankhead, C.; Sharp, D. Risk of Ovarian Cancer in Women with Symptoms in Primary Care: Population-Based Case-Control Study. *Br. Med. J.* **2009**, *339*, b2998.

(2) Będkowska, G. E.; Ławicki, S.; Gacuta, E.; Pawłowski, P.; Szmitkowski, M. M-CSF in A New Biomarker Panel with HE4 And CA 125 in The Diagnostics of Epithelial Ovarian Cancer Patients. *J. Ovarian Res.* **2015**, *8*, 27.

(3) Scholler, N.; Crawford, M.; Sato, A.; Drescher, C. W.; O'Briant, K. C.; Kiviat, N.; Anderson, G. L.; Urban, N. Bead-Based ELISA for Validation of Ovarian Cancer Early Detection Markers. *Clin. Cancer Res.* **2006**, *12*, 2117−2124.

(4) Zhu, Q.; Chai, Y.; Zhuo, Y.; Yuan, R. Ultrasensitive Simultaneous Detection of Four Biomarkers Based On Hybridization Chain Reaction And Biotinestreptavidin Signal Amplification Strategy. *Biosens. Bioelectron.* **2015**, *68*, 42−48.

(5) Lamberti, I.; Scarano, S.; Esposito, C. L.; Antoccia, A.; Antonini, G.; Tanzarella, C.; De Franciscis, V.; Minunni, M. In Vitro Selection of RNA Aptamers Against CA125 Tumor Marker In Ovarian Cancer And Its Study By Optical Biosensing. *Methods* **2016**, *97*, 58−68.

(6) Yin, Y.; Cao, Y.; Xu, Y.; Li, G. Colorimetric Immunoassay for Detection of Tumor Markers. *Int. J. Mol. Sci.* **2010**, *11*, 5077−5094.

(7) Wu, S.; Xu, K.; Chen, G.; Zhang, J.; Liu, Z.; Xie, X. Identification of Serum Biomarkers For Ovarian Cancer Using Maldietof-MS Combined With Magnetic Beads. *Int. J. Clin. Oncol.* **2012**, *17*, 89−95.

(8) Ricci, F.; Adornetto, G.; Palleschi, G. A Review of Experimental Aspects of Electrochemical Immunosensors. *Electrochim. Acta* **2012**, *84*, 74−83.

(9) Pei, X.; Zhang, B.; Tang, J.; Liu, B.; Lai, W.; Tang, D. Sandwich-Type Immunosensors And Immunoassays Exploiting Nanostructure Labels: A Review. *Anal. Chim. Acta* **2013**, *758*, 1−18.

(10) Razmi, N.; Hasanzadeh, M. Current Advancement on Diagnosis of Ovarian Cancer Using Biosensing of CA 125 Biomarker: Analytical Approaches. *TrAC, Trends Anal. Chem.* **2018**, *108*, 1−12.

(11) Johari-Ahar, M.; Rashidi, M. R.; Barar, J.; Aghaie, M.; Mohammadnejad, D.; Ramazani, A.; Karami, P.; Coukos, G.; Omidi, Y. An Ultra-Sensitive Impedimetric Immunosensor for Detection of the Serum Oncomarker CA 125 in Ovarian Cancer Patients. *Nanoscale* **2015**, *7*, 3768−3779.

(12) Jafari, M.; Hasanzadeh, M.; Solhi, E.; Hassanpour, S.; Shadjou, N.; Mokhtarzadeh, A.; Jouyban, A.; Mahboob, S. Ultrasensitive Bioassay of Epitope of Mucin-16 Protein (CA 125) in Human Plasma Samples Using A Novel Immunoassay Based on Silver Conductive Nano-Ink: A New Platform in Early Stage Diagnosis of Ovarian Cancer And Efficient Management. *Int. J. Biol. Macromol.* **2019**, *126*, 1255−1265.

(13) Bangar, M. A.; Shirale, D. J.; Chen, W.; Myung, N. V.; Mulchandani, A. Single Conducting Polymer Nanowire Chemiresistive Label-Free Immunosensor for Cancer Biomarker. *Anal. Chem.* **2009**, *81*, 2168−2175.

(14) Yang, Z.; Xie, Z.; Liu, H.; Yan, F.; Ju, H. Streptavidin-Functionalized Three-Dimensional Ordered Nanoporous Silica Film for Highly Efficient Chemiluminescent Immunosensing. *Adv. Funct. Mater.* **2008**, *18*, 3991−3998.

(15) Lu, J.; Liu, S.; Ge, S.; Yan, M.; Yu, J.; Hu, X. Ultrasensitive Electrochemical Immunosensor Based on Au Nanoparticles Dotted Carbon Nanotube-Graphene Composite And Functionalized Mesoporous Materials. *Biosens. Bioelectron.* **2012**, *33*, 29−35.

(16) Majd, S. M.; Salimi, A. Ultrasensitive Flexible FET-Type Aptasensor For CA 125 Cancer Marker Detection Based on Carboxylated Multiwalled Carbon Nanotubes Immobilized Onto Reduced Graphene Oxide Film. *Anal. Chim. Acta* **2018**, *1000*, 273−282.

(17) Pachfule, P.; Das, R.; Poddar, P.; Banerjee, R. Solvothermal Synthesis, Structure, and Properties of Metal-Organic Framework Isomers Derived from a Partially Fluorinated Link. *Cryst. Growth Des.* **2011**, *11*, 1215−1222.

(18) Xuan, W.; Zhu, C.; Liu, Y.; Cui, Y. Mesoporous Metal-Organic Framework Materials. *Chem. Soc. Rev.* **2012**, *41*, 1677−1695.

(19) Lee, J.; Farha, O. K.; Roberts, J.; Scheidt, K. A.; Nguyen, S. T.; Hupp, J. T. Metal-Organic Framework Materials as Catalysts. *Chem. Soc. Rev.* **2009**, *38*, 1450−1459.

(20) Kreno, L. E.; Leong, K.; Farha, O. K.; Allendorf, M.; Van Duyne, R. P.; Hupp, J. T. Metal-Organic Framework Materials as Chemical Sensors. *Chem. Rev.* **2012**, *112*, 1105−1125.

(21) Zornoza, B.; Tellez, C.; Coronas, J.; Gascon, J.; Kapteijn, F. Metal-Organic Framework Based Mixed Matrix Membranes: An Increasingly Important Field of Research With A Large Application Potential. *Microporous Mesoporous Mater.* **2013**, *166*, 67−78.

(22) Wang, X.; Wang, Q.; Wang, Q.; Gao, F.; Gao, F.; Yang, Y.; Guo, H. Highly Dispersible and Stable Copper Terephthalate Metal-Organic Framework-Graphene Oxide Nanocomposite for an Electrochemical Sensing Application. *ACS Appl. Mater. Interfaces* **2014**, *6*, 11573−11580.

(23) Chen, Y.; Lykourinou, V.; Vetromile, C.; Hoang, T.; Ming, L.-J.; Larsen, R. W.; Ma, S. How Can Proteins Enter The Interior Of A MOF? Investigation of Cytochrome C Translocation into A MOF Consisting Of Mesoporous Cages with Microporous Windows. *J. Am. Chem. Soc.* **2012**, *134*, 13188−13191.

(24) Liu, W.-L.; Lo, S.-H.; Singco, B.; Yang, C.-C.; Huang, H.-Y.; Lin, C.-H. Novel Trypsin-FITC@MOF Bioreactor Efficiently Catalyzes Protein Digestion. *J. Mater. Chem. B* **2013**, *1*, 928−932.

(25) Lian, X.; Fang, Y.; Joseph, E.; Wang, Q.; Li, J.; Banerjee, S.; Lollar, C.; Wang, X.; Zhou, H.-C. Enzyme-MOF (Metal-Organic Framework) Composites. *Chem. Soc. Rev.* **2017**, *46*, 3386−3401.

(26) Ly, H. G. T.; Fu, G.; Kondinski, A.; Bueken, B.; De Vos, D.; Parac-Vogt, T. N. Superactivity of MOF-808 toward Peptide Bond Hydrolysis. *J. Am. Chem. Soc.* **2018**, *140*, 6325−6335.

(27) Absillis, G.; Parac-Vogt, T. N. Peptide Bond Hydrolysis Catalyzed by the Wells−Dawson Zr(α2-P2W17O61)2 Polyoxometalate. *Inorg. Chem.* **2012**, *51*, 9902−9910.

(28) Zheng, H.-Q.; Liu, C.-Y.; Zeng, X.-Y.; Chen, J.; Lü, J.; Lin, R.-G.; Cao, R.; Lin, Z.-J.; Su, J.-W. MOF-808: A Metal-Organic Framework with Intrinsic Peroxidase Like Catalytic Activity at Neutral pH for Colorimetric Biosensing. *Inorg. Chem.* **2018**, *57*, 9096−9104.

(29) Jiang, J.; Gándara, F.; Zhang, Y.-B.; Na, K.; Yaghi, O. M.; Klemperer, W. G. Superacidity in Sulfated Metal-Organic Framework-808. *J. Am. Chem. Soc.* **2014**, *136*, 12844−12847.

(30) Furukawa, H.; Gándara, F.; Zhang, Y.-B.; Jiang, J.; Queen, W. L.; Hudson, M. R.; Yaghi, O. M. Water Adsorption in Porous Metal-Organic Frameworks and Related Materials. *J. Am. Chem. Soc.* **2014**, *136*, 4369−4381.
(31) Likodimos, V.; Steriotis, T. A.; Papageorgiou, S. K.; Romanos, G. E.; Marques, R. R. N.; Rocha, R. P.; Faria, J. L.; Pereira, M. F. R.; Figueiredo, J. L.; Silva, A. M. T.; Falaras, P. Controlled Surface Functionalization of Multiwall Carbon Nanotubes By HNO_3 Hydrothermal Oxidation. *Carbon* **2014**, *69*, 311−326.
(32) Liu, H.; Zhang, Z.; Tang, J.; Fei, Z.; Liu, Q.; Chen, X.; Cui, M.; Qiao, X. Quest For Pore Size Effect on The Catalytic Property of Defect-Engineered MOF-808-SO_4 in The Addition Reaction of Isobutylene With Ethylene Glycol. *J. Solid State Chem.* **2019**, *269*, 9−15.
(33) Huang, J.; Yang, G.; Meng, W.; Wu, L.; Zhu, A.; Jiao, X. A. An Electrochemical Impedimetric Immunosensor For Label-Free Detection of Campylobacter Jejuni in Diarrhea Patients' Stool Based on O-Carboxymethylchitosan Surface Modified Fe3O4 Nanoparticles. *Biosens. Bioelectron.* **2010**, *25*, 1204−1211.
(34) Biswas, S.; Chen, Y.; Xie, Y.; Sun, X.; Wang, Y. Ultra-Small Au(0) Inserted Hollow PCN-222 MOF for The High-Sensitive Detection of Estradiol. *Anal. Chem.* **2020**, *92*, 4566−4572.
(35) Hamd-Ghadareh, S.; Abdollah, S.; Fardin, F.; Saman, B. An Amplified Comparative Fluorescence Resonance Energy Transfer Immunosensing of CA 125 Tumor Marker And Ovarian Cancer Cells Using Green And Economic Carbon Dots For Bio-Applications In Labeling, Imaging And Sensing. *Biosens. Bioelectron.* **2017**, *96*, 308−316.
(36) Zhang, K.; Shen, X. Cancer Antigen 125 Detection Using the Plasmon Resonance Scattering Properties of Gold Nanorods. *Analyst* **2013**, *138*, 1828−1834.
(37) Li, M.; Zhang, M.; Ge, S.; Yan, M.; Yu, J.; Huang, J.; Liu, S. Ultrasensitive Electrochemiluminescence Immunosensor Based on Nanoporous Gold Electrode And Ru-Aunps/Graphene as Signal Labels. *Sens. Actuators, B* **2013**, *181*, 50−56.
(38) Zhao, Y.; Zheng, Y.; Zhao, C.; You, J.; Qu, F. Hollow PDA-Au Nanoparticles-Enabled Signal Amplification For Sensitive Non-enzymatic Colorimetric Immunodetection of Carbohydrate Antigen 125. *Biosens. Bioelectron.* **2015**, *71*, 200−206.
(39) Fan, Y.; Shi, S.; Ma, J.; Guo, Y. A Paper-Based Electrochemical Immunosensor with Reduced Graphene Oxide/Thionine/Gold Nanoparticles Nanocomposites Modification for the Detection of Cancer Antigen 125. *Biosens. Bioelectron.* **2019**, *135*, 1−7.

https://dx.doi.org/10.1021/acsami.0c14946
ACS Appl. Mater. Interfaces 2021, 13, 3295−3302